materials

MDPI

Article

Structure and Optical Properties of TiO_2 Films Prepared by Electron Beam Evaporation of Al_2O_3-Doped Ti_3O_5

Cheng Peng [1,2,3,4,*], Xingqi Wang [1,2,3], Zhixia Shi [1,2,3], Huaying Duan [1,2,3], Bitian Zhang [1,2,3] and Yanxi Yin [1,2,3,4,*]

[1] National Engineering Research Center for Environment-Friendly Metallurgy in Producing Premium Non-Ferrous Metals, GRINM Group Corporation Limited, Beijing 101407, China
[2] GRINM Resources and Environment Tech. Co., Ltd., Beijing 101407, China
[3] Beijing Engineering Research Center of Strategic Nonferrous Metals Green Manufacturing Technology, Beijing 101407, China
[4] General Research Institute for Nonferrous Metals, Beijing 100088, China
* Correspondence: pengcheng@grinm.com (C.P.); yinyanxi@grinm.com (Y.Y.)

Highlights

What are the main findings?

- Al_2O_3 doping stabilizes high-temperature stable λ-Ti_3O_5 to room temperature, with complete β→λ phase transition at 5 at% doping content.
- 12.5 at% Al_2O_3 doping is determined as the optimal content, balancing stable composition transfer, low extinction coefficient, and moderate refractive index for TiO_2 films.
- Al_2O_3 doping continuously reduces TiO_2 film refractive index/extinction coefficient, while increasing optical band gap and surface roughness.

What are the implications of the main findings?

- The phase transition regulation mechanism via Al^{3+}-induced lattice contraction/distortion is revealed, guiding Ti_3O_5-based material design.
- This work provides experimental/theoretical support for TiO_2 film doping modification and high-performance optical filter applications.

Abstract

The crystal structure regulation of Ti_3O_5 by Al_2O_3 doping and its effect on the optical properties of TiO_2 films prepared by electron beam evaporation were systematically studied. Ti_3O_5 coating materials with different Al_2O_3 doping contents (0–50 at%) were prepared by vacuum melting, and the corresponding TiO_2 films were deposited on K9 glass substrates via electron beam vacuum evaporation. The phase structure, phase transition temperature, chemical composition and optical properties of the materials and films were characterized by XRD, DSC, EDS, XPS, UV-Vis and AFM. Results show that Al_2O_3 doping induces the phase transition of Ti_3O_5 from a room-temperature stable β-phase to a high-temperature stable λ-phase, with complete transition at 5 at% doping. Al^{3+} with a smaller ionic radius causes lattice contraction and local distortion of Ti_3O_5, enabling stabilization at room temperature of the λ-phase. For TiO_2 films, 12.5 at% doping is the optimal state with the stable composition transfer under this condition. With the increase in Al_2O_3 doping content, the refractive index and extinction coefficient of TiO_2 films decrease continuously, while the optical band gap and surface roughness show an increasing trend. The changes in optical properties are mainly ascribed to the low refractive index of Al_2O_3, lattice compressive strain effect and oxygen vacancy passivation induced by Al^{3+}. This study clarifies the regulation effect of Al_2O_3 doping on Ti_3O_5 phase transition and TiO_2 film optical properties, and provides theoretical basis and experimental reference for the doping modification of TiO_2 films and their practical applications in consumer electronics and optical filter devices.

Check for updates

Academic Editor: Kamalan Kirubaharan Amirtharaj Mosas

Received: 20 March 2026
Revised: 10 April 2026
Accepted: 14 April 2026
Published: 17 April 2026

Copyright: © 2026 by the authors. Licensee MDPI, Basel, Switzerland. This article is an open access article distributed under the terms and conditions of the Creative Commons Attribution (CC BY) license.

Keywords: Ti_3O_5; Al_2O_3 doping; electron beam evaporation; TiO_2 films; optical properties

1. Introduction

TiO_2 films with excellent optical transparency and chemical stability are widely used as high-refractive-index materials in optical filters, anti-reflection coatings and other optical devices for the visible and near-infrared spectrum. Reactive electron beam evaporation using Ti_3O_5 as the coating raw material is an effective method to prepare high-quality TiO_2 films, which has the advantages of low evaporation temperature, stable oxygen content and easy preparation of stoichiometric and highly reproducible TiO_2 films [1]. However, Ti_3O_5 undergoes a reversible solid-state phase transition from β-phase (room-temperature stable) to λ-phase (high-temperature stable) during heating and cooling. This phase transition causes crystal volume expansion and contraction, leading to material cracking and splashing during evaporation, which seriously affects the surface smoothness and optical performance of the prepared TiO_2 films.

Doping modification is an effective strategy to stabilize the high-temperature stable λ-Ti_3O_5 phase to room temperature and suppress its phase transition. Existing research on Ti_3O_5 doping mainly focuses on the preparation and functional application of doped λ-Ti_3O_5. Nakamura et al. [2] calculated the binding energy of 54 metal-doped λ-Ti_3O_5 and prepared Sc-doped λ-Ti_3O_5 for thermal energy storage research. Shen et al. [3] prepared Al-doped λ-Ti_3O_5 by carbothermal reduction and studied the effect of Al doping on the electrical resistance of λ-Ti_3O_5. Wang et al. [4] investigated the phase evolution law of Mg-doped Ti_3O_5 and the formation mechanism of λ-phase. For TiO_2 film preparation, various methods such as sol–gel, electron beam evaporation and magnetron sputtering have been widely used, and doping modification is often adopted to regulate its optical properties for photocatalysis, photovoltaics and other applications. Ahmad et al. [5] prepared Mg/Ni/Sn-doped TiO_2 films by sol–gel dip-coating and systematically studied the regulation of metal doping on the structure and optical/electrical properties of TiO_2 films. Rehman et al. [6] prepared $TiO_2/V_2O_5/TiO_2$ multilayer films by electron beam evaporation and analyzed the changes in band gap width and thermal stability. Ogawa et al. [7] studied the effect of oxygen content on the photocatalytic activity of TiO_2 films prepared by magnetron sputtering.

However, there is a lack of systematic research on the component transfer stability of Al_2O_3-stabilized Ti_3O_5 coating materials during electron beam vacuum evaporation, as well as the specific influence mechanism of Al ions on the optical band gap, absorption coefficient and surface morphology of TiO_2 films. In this work, Al_2O_3-doped Ti_3O_5 coating materials with different doping contents were prepared by vacuum melting, and TiO_2 films were deposited on K9 substrates by electron beam evaporation. The inhibitory effect of Al_2O_3 doping on Ti_3O_5 phase transition was clarified, and the influence rule of Al_2O_3 doping content on the chemical composition, surface morphology and optical properties of TiO_2 films was revealed. This study provides a theoretical basis and experimental reference for the optimization of TiO_2 film preparation process and its application in high-performance optical devices.

2. Materials and Methods

2.1. Experimental Materials

High-purity TiO_2, Ti and Al_2O_3 powders (4N grade, Sinopharm Group Chemical Reagent Co., Ltd., Shanghai, China) were used as raw materials. The molar ratio of TiO_2 to Ti powder was fixed at 9:1 to synthesize Ti_3O_5. The raw materials were uniformly

mixed according to the Al_2O_3/TiO_2 molar ratios of 0, 0.5%, 1.5%, 2.5%, 5%, 12.5% and 50%. Al_2O_3-doped Ti_3O_5 coating materials were prepared by high-temperature melting in a vacuum furnace at 1800 °C under a vacuum of 10^{-1}~10^{-2} Pa.

2.2. Preparation of Al_2O_3-Doped TiO_2 Films

Al_2O_3-doped TiO_2 films were prepared by electron beam vacuum evaporation using a ZZS900 type vacuum coating machine (Chengdu Vacuum Machinery Factory, Chengdu, China). K9 glass was used as the substrate (China Southern Glass Co., Ltd., Chengdu, China), and the base vacuum of the coating chamber was pumped to 3×10^{-3} Pa. The substrate temperature was set to 100 °C during evaporation, and high-purity oxygen was introduced to control the chamber vacuum at 1×10^{-2} Pa. The evaporation parameters were as follows: high voltage 8 KV, evaporation rate 0.3 nm/s (controlled by XTC/3M, INFICON Inc., East Syracuse, NY, USA, and substrate rotation speed 15 r/min to ensure uniform film deposition. The samples were stored in PVC bags and measured within 72 h.

2.3. Material Performance Characterization

2.3.1. Material Phase and Phase Transition Temperature Testing

The phase composition of Al_2O_3-doped Ti_3O_5 was analyzed by an X-ray diffractometer (XRD, D8Advance, Bruker Corporation, Billerica, MA, USA) with Cu Kα monochromatic X-ray source (wavelength 1.54056 Å). The test conditions were: scan range 10–90°, scan rate 5°/min, step size 0.01°. The phase transition temperature of doped Ti_3O_5 was characterized by a simultaneous thermal analyzer (DSC, 449F-1, Netzsch-Gerätebau GmbH, Selb, Germany) with thermogravimetry and differential scanning calorimetry functions. The test was carried out in Ar atmosphere with a maximum temperature of 300 °C and a heating rate of 10 °C/min. The chemical composition and element distribution of the materials were analyzed by energy dispersive spectroscopy (EDS, FEI Tecnai G2 F3, Oxford Instruments, Abingdon, UK).

2.3.2. Film Performance Analysis

The transmittance of TiO_2 films in the ultraviolet to near-infrared region was measured by a UV-visible spectrophotometer (UV2600, Shimadzu Corporation, Kyoto, Japan) with a wavelength range of 300–800 nm. The surface chemical composition and element valence state of the films were analyzed by X-ray photoelectron spectroscopy (XPS, ESCALAB 250Xi, Thermo Fisher Scientific, Waltham, MA, USA). XPS measurements were performed using an Al Kα X-ray source with a photon energy of 1486.6 eV. The photoelectron emission angle was set to 90° relative to the sample surface normal, and the analyzed area was 500×500 μm^2. The samples were placed in the analysis chamber without direct contact with the spectrometer. No sputter-etching was performed prior to analysis. The base pressure in the analysis chamber during measurements was 1×10^{-9} mbar, and a charge neutralizer was employed during data acquisition. The survey scan energy range is 0–1350 eV (High-resolution scan: Ti 2p: 448–475 eV, O 1s: 523–541 eV, C 1s: 276–298 eV, Al 2p: 65–85 eV). The surface morphology and roughness of the films were characterized by atomic force microscopy (AFM, Dimension Edge, Bruker Corporation, Billerica, MA, USA).

3. Results and Discussion

3.1. Regulation of Al_2O_3 Doping on Ti_3O_5 Crystal Structure and Thermodynamic Phase Transition

The XRD results of Ti_3O_5 doped with different Al_2O_3 contents (Figure 1) show that with the increase in Al_2O_3 doping content, the diffraction peak intensity of β-Ti_3O_5 gradu-

ally decreases, and the λ-Ti_3O_5 begins to appear and its intensity gradually increases. The phase composition of Ti_3O_5 after different Al_2O_3 doping is shown in Table 1.

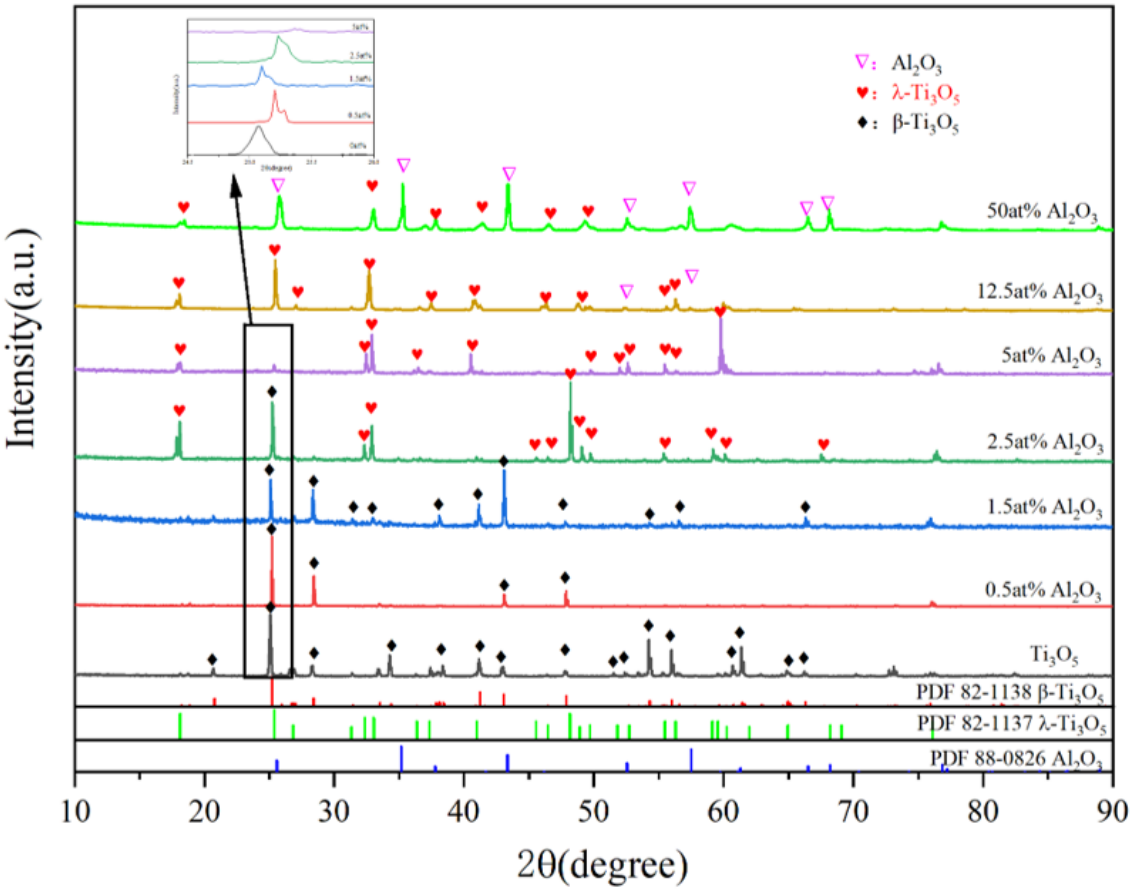


Figure 1. XRD results of Ti_3O_5 doped with different Al_2O_3 contents.

Table 1. Phase composition of Ti_3O_5 after doping with different contents of Al_2O_3.

Al_2O_3 Doping Content/at%	Phase Composition
0	β-Ti_3O_5
0.5	β-Ti_3O_5
1.5	β-Ti_3O_5
2.5	β-Ti_3O_5 + λ-Ti_3O_5
5	λ-Ti_3O_5
12.5	λ-Ti_3O_5 + trace Al_2O_3
50	λ-Ti_3O_5 + Al_2O_3

When the Al_2O_3 doping content is 0.5 at% and 1.5 at%, no λ-Ti_3O_5 is observed, but the position of the strong diffraction peak of β-Ti_3O_5 changes slightly compared with the pure sample, indicating that Al^{3+} has entered the Ti_3O_5 lattice and caused lattice distortion. When the doping content reaches 2.5 at%, the λ-Ti_3O_5 begins to appear, and most of the λ-phase is stabilized to room temperature. When the doping content is 5 at%, the β-Ti_3O_5 completely transforms into the λ-Ti_3O_5, realizing the complete room-temperature stabilization of the high-temperature phase. With the further increase in doping content to 12.5 at%, trace Al_2O_3 phase precipitates at the grain boundaries, and a large amount of Al_2O_3 phase appears when the doping content reaches 50 at%, which is due to the excess Al^{3+} that cannot enter the Ti_3O_5 lattice and forms the second phase. The structural parameters of β-Ti_3O_5, λ-Ti_3O_5, and Al_2O_3 are show in Table 2.

Table 2. Structural parameters of β-Ti_3O_5, λ-Ti_3O_5, and Al_2O_3 phases.

Phase	Crystal Structure	Space Group	a	b	c	β	V
β-Ti_3O_5	Monoclinic	C2/m	9.7568	3.8008	9.4389	91.547	349.9
λ-Ti_3O_5	Monoclinic	C2/m	9.8261	3.7894	9.9694	91.258	371.12
Al_2O_3	Hexagonal	R-3c	4.7607	4.7607	12.997	120	255.1

The crystal structure data according to PDF cards, β-Ti_3O_5: No. 82-1138, λ-Ti_3O_5: No. 82-1137, Al_2O_3: No. 88-0826.

Comparing the characteristic peak of β-Ti_3O_5 at 2θ = 25.1°, the diffraction peak shifts to a higher diffraction angle with the increase in Al_2O_3 doping content. According to Bragg's law (Formula (1)), the interplanar spacing d decreases with the increase in diffraction angle θ, indicating that Al_2O_3 doping causes the lattice contraction of Ti_3O_5.

$$2d\sin\theta = n\lambda \quad (1)$$

where d is the interplanar spacing, θ is the diffraction angle, n is the diffraction order, λ is the X-ray wavelength.

The crystal structure of Ti_3O_5 is constructed with TiO_6 octahedra as the basic structural unit, which forms a three-dimensional framework through edge and corner sharing (Figure 2) [8]. Ti ions are located at the octahedral center with six-coordinate configuration, and the ionic radii of Ti^{3+} and Ti^{4+} are 0.67 Å and 0.605 Å, respectively, while the ionic radius of doped Al^{3+} is only 0.535 Å, with a radius difference of about 20–25% compared with Ti ions. When Al^{3+} replaces the larger Ti^{3+}/Ti^{4+} in the lattice, it causes the contraction of the local TiO_6 octahedral structure, leading to the micro-adjustment of the lattice parameters of the entire unit cell. The difference in ionic radius leads to the non-uniform change in the bond length and bond angle of the TiO_6 octahedron (the Al-O bond length is 1.91 Å, shorter than the Ti-O bond length of 2.0–2.1 Å), forming local lattice distortion. This distortion only exists in the short-range surrounding of Al^{3+} and does not damage the integrity of the overall three-dimensional framework under appropriate doping content, thus helping to stabilize the high-temperature stable λ-Ti_3O_5 to room temperature.

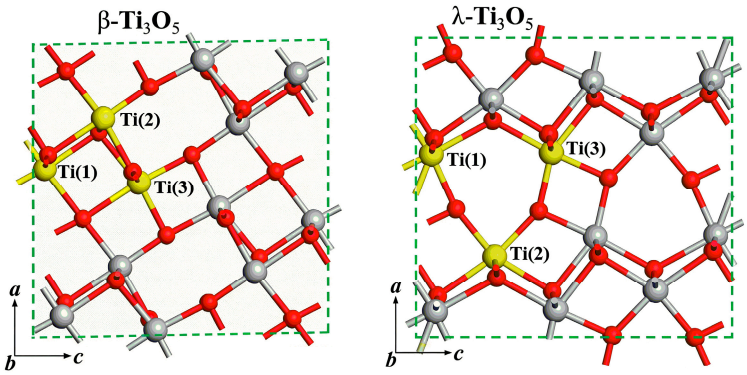


Figure 2. Crystal structure diagrams of β-Ti_3O_5 and λ-Ti_3O_5.

At the doping levels ranging from 0.5 at% to 5 at%, Al^{3+} is uniformly dispersed at the Ti ion sites in the lattice, and the local lattice distortions cancel each other out, resulting in uniform contraction of the unit cell and basically unchanged crystallinity of the material. At high doping levels, the excess Al^{3+} cannot fully enter the Ti_3O_5 lattice, and the undoped Al^{3+} forms the Al_2O_3 second phase at the grain boundaries, which is consistent with the XRD results of 12.5 at% and 50 at% doping samples.

The DSC analysis results of pure Ti_3O_5 and 5 at% Al_2O_3-doped Ti_3O_5 (Figure 3) show the significant regulation effect of Al_2O_3 doping on the phase transition performance of

Ti_3O_5. Pure Ti_3O_5 begins to undergo phase transition at about 184 °C during heating, which is an endothermic process. The β-phase is the low-temperature stable phase, and its transformation to the high-temperature stable λ-phase needs to absorb heat to overcome the phase transition energy barrier and drive the atomic rearrangement (such as the formation of Ti-Ti dimers [9]). The λ-phase is stable at high temperature, and when the temperature decreases, it spontaneously transforms back to the β-phase and releases heat, showing an exothermic peak at 174–160 °C. For the Ti_3O_5 material with 5 at% Al_2O_3 doping, only a very weak endothermic peak appears at 141.0–151.4 °C, and the signal is close to the baseline, indicating that the phase transition degree of the doped sample is extremely low and the phase composition is stable at room temperature and heating process.

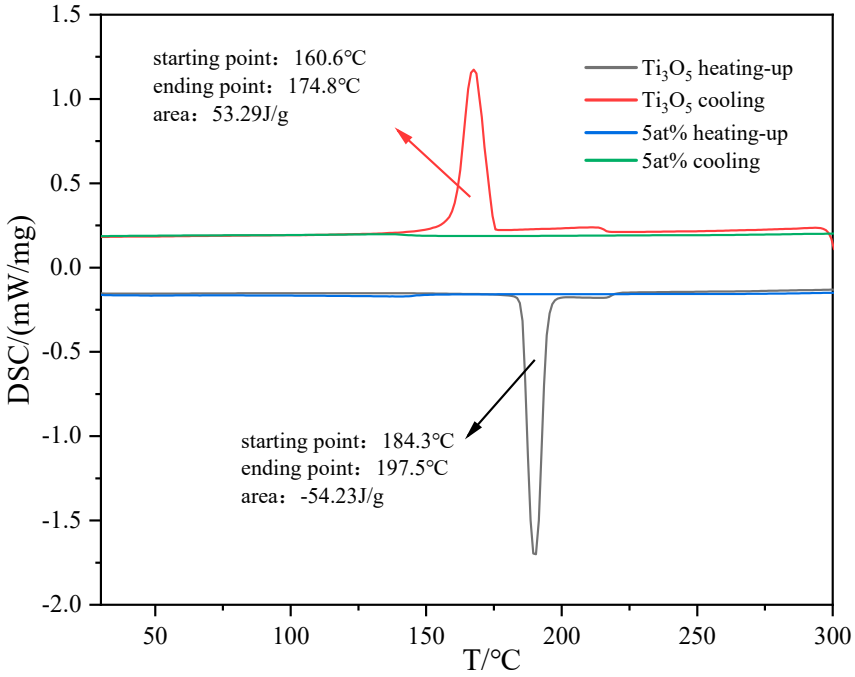


Figure 3. DSC curves of pure Ti_3O_5 and 5 at% Al_2O_3-doped Ti_3O_5.

The EDS results of 5 at% Al_2O_3-doped Ti_3O_5 (Figure 4) show that Al element is uniformly distributed in the Ti_3O_5 matrix, and the energy spectrum test result of Al/Ti atomic ratio is 1/10, which is close to the theoretical ratio of Al_2O_3/TiO_2 = 5 at%, indicating that Al_2O_3 is uniformly doped in the Ti_3O_5 material during the vacuum melting process without obvious element segregation.

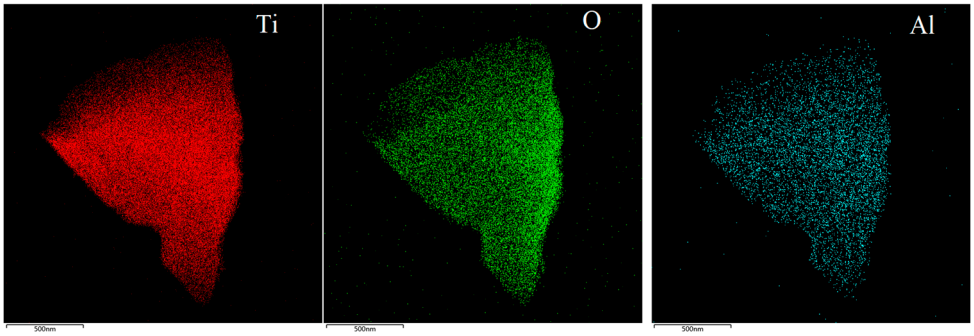


Figure 4. *Cont.*

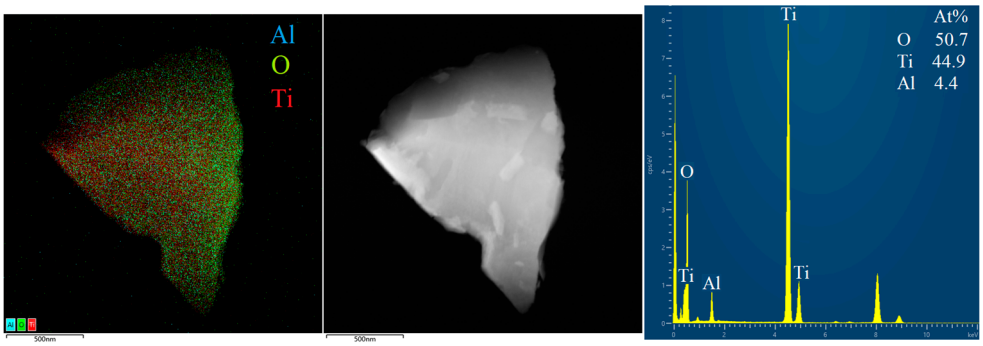


Figure 4. EDS mapping and spectrum of 5 at% Al_2O_3-doped Ti_3O_5.

3.2. Film Chemical Composition and Valence State

To further investigate the effect of Al_2O_3 doping on the properties of TiO_2 thin films, Al_2O_3-doped TiO_2 thin films were prepared. The XPS analysis was used to characterize the surface chemical composition and element valence state of TiO_2 films prepared from Ti_3O_5 with different Al_2O_3 doping contents. The XPS full spectrum and characteristic peak curves are shown in Figure 5.

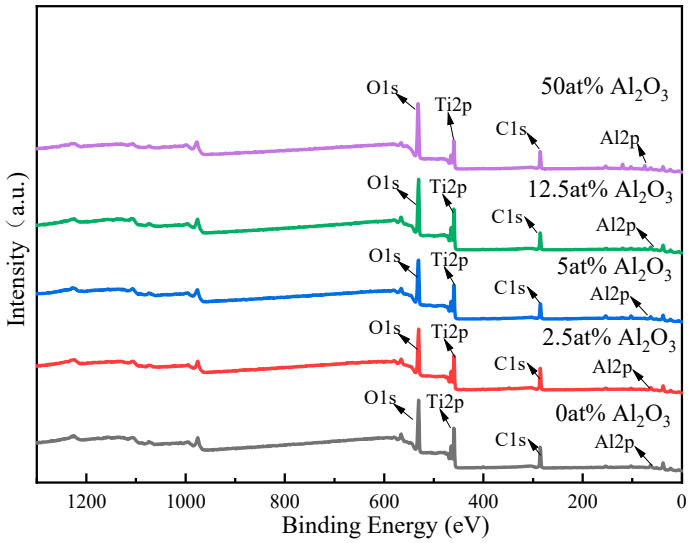


Figure 5. XPS survey spectra of TiO_2 films with different Al_2O_3 doping contents.

The binding energy calibration was carefully revised with consideration of the sample work function. The work function of TiO_2 (ΦSA = 4.22 eV) was taken from the literature [10]. The corrected C 1s reference position was calculated as BE = 289.58 − ΦSA = 285.36 eV. The energy shift was determined from the difference between the measured C 1s binding energy and the corrected BE, and this shift was applied to all core-level spectra. High-resolution spectra of C 1s, O 1s, Ti 2p, and Al 2p were deconvoluted via peak fitting, and the detailed fitting results are presented in Figure 6.

Figure 6a shows the C 1s high-resolution spectra were deconvoluted into two distinct components for all samples. A dominant peak centered at ~285.4 eV, assigned to the C–C bond, which served as the internal reference for charge correction. A weak peak at ~289 eV, attributed to the O–C=O bond from trace surface carbon contamination [11]. No significant shift in the C–C peak position was observed across all doping concentrations, confirming the consistency of charge correction throughout the series.

Figure 6b shows the O 1s spectra were fitted with two components. A main peak at ~530.8 eV, corresponding to lattice oxygen in Ti–O bonds of the TiO_2 matrix. A secondary

peak at ~532.6 eV, assigned to C–O bonds from surface adsorbed oxygen and residual carbon contamination. The Ti–O peak position remained stable with increasing Al_2O_3 content, indicating that Al^{3+} doping did not significantly alter the chemical environment of Ti–O bonds in the TiO_2 lattice.

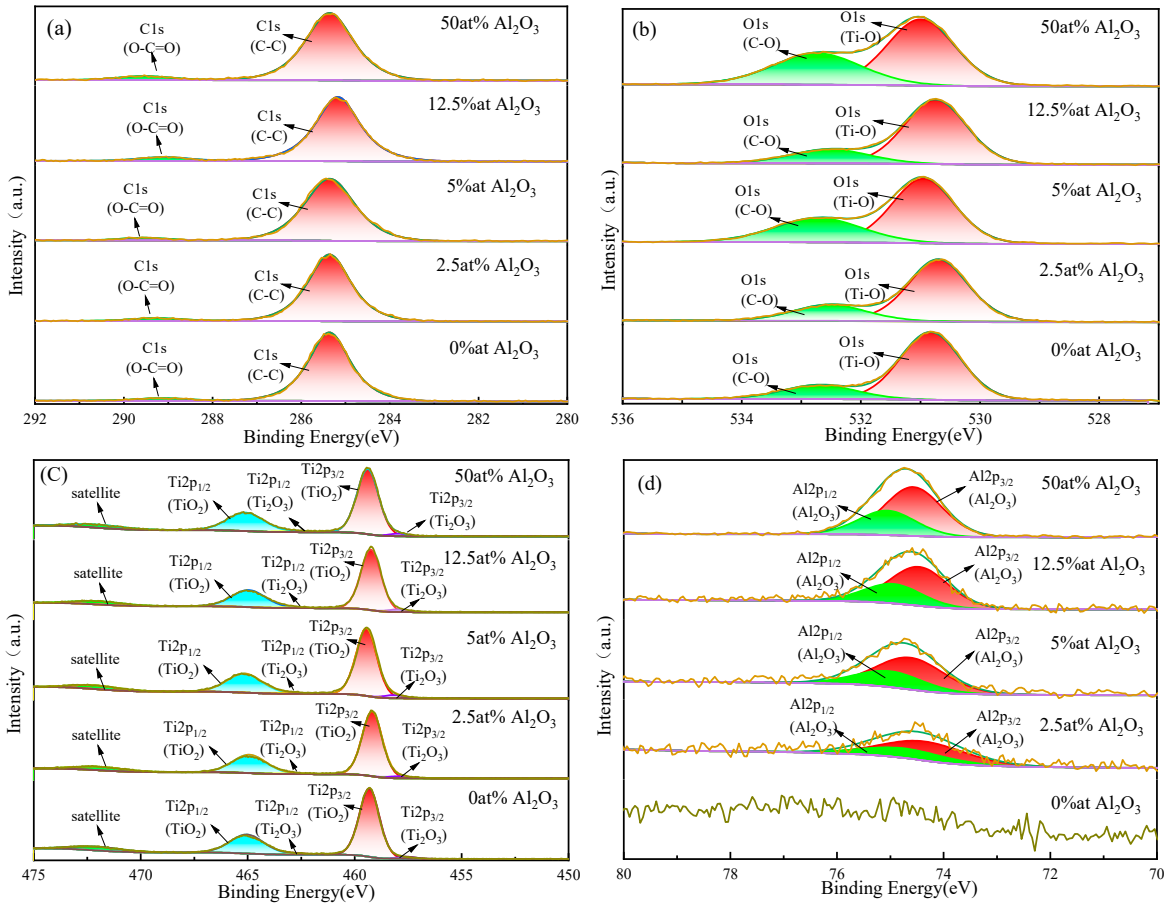


Figure 6. XPS high-resolution spectra of C 1s (**a**), O 1s (**b**), Ti 2p (**c**) and Al 2p (**d**) for TiO_2 films with different Al_2O_3 doping contents.

Figure 6c shows The Ti 2p spectra were deconvoluted into spin–orbit split doublets for Ti^{4+} (TiO_2) and Ti^{3+} (Ti_2O_3). Ti^{4+}: Ti $2p_3/_2$ at ~459 eV and Ti $2p_1/_2$ at ~464.8 eV, which was the dominant component in all samples, confirming the TiO_2 phase as the main matrix. Ti^{3+}: Ti $2p_3/_2$ at ~457.7 eV and Ti $2p_1/_2$ at ~463.5 eV, a minor component attributed to intrinsic oxygen vacancies in TiO_2. A weak satellite peak was observed at ~472 eV.

Figure 6d shows the Al 2p spectra were only detectable in Al_2O_3-doped samples (0 at% Al_2O_3 showed no Al signal), and were fitted with spin–orbit split peaks for Al^{3+} in Al_2O_3: Al $2p_3/_2$ at ~74.5 eV and Al $2p_1/_2$ at ~74.9 eV, confirming that Al was incorporated into the TiO_2 matrix in the form of Al_2O_3. The peak intensity of Al 2p increased monotonically with increasing Al_2O_3 content, while the peak position remained stable, verifying the successful and uniform doping of Al_2O_3 into the TiO_2 thin films without the formation of other aluminum-containing impurity phases.

The quantitative XPS results, including atomic percentages of Ti, O, Al, and their respective chemical state ratios, are summarized in Table 3, providing a comprehensive overview of the elemental composition and chemical state evolution with Al_2O_3 doping.

Table 3. Chemical composition of TiO_2 films prepared from Ti_3O_5 doped with different contents of Al_2O_3.

Sample	Peak	Position/eV	FWHM/eV	Assignment	Atomic Ratio/at%	Al_2O_3/TiO_2 at% (Calculate)
0 at% Al_2O_3	C 1s	285.36	1.1	Adventitious C	/	0
	O1s	530.83	1.21	Lattice O (Ti–O/Al–O)	46.27	
	O1s-2	532.7	1.44	O-C=O	11.57	
	$Ti2p_{3/2}$-1	459.31	1.15	Ti^{4+}	20.48	
	$Ti2p_{1/2}$-1	465.02	1.94	Ti^{4+}	18.88	
	$Ti2p_{3/2}$-2	457.58	1.09	Ti^{3+}	0.53	
	$Ti2p_{1/2}$-2	462.84	1.42	Ti^{3+}	0.38	
	Ti2p	472.03	2.81	satellite, Ti^{4+}	1.9	
2.5 at% Al_2O_3	C 1s	285.36	1.14	Adventitious C	/	6.1
	$Al2p_{3/2}$	74.35	1.85	Al^{3+} (Al_2O_3)	2.45	
	$Al2p_{1/2}$	74.74	1.85	Al^{3+} (Al_2O_3)	2.45	
	O1s	530.7	1.19	Lattice O (Ti–O/Al–O)	43.78	
	O1s-2	532.52	1.44	O-C=O	13.62	
	$Ti2p_{3/2}$-1	459.2	1.11	Ti^{4+}	18.02	
	$Ti2p_{1/2}$-1	464.92	1.86	Ti^{4+}	16.61	
	$Ti2p_{3/2}$-2	457.89	1.29	Ti^{3+}	0.72	
	$Ti2p_{1/2}$-2	462.99	2.16	Ti^{3+}	0.66	
	Ti2p	471.88	2.78	satellite, Ti^{4+}	1.69	
5 at% Al_2O_3	C 1s	285.36	1.34	Adventitious C	/	10.7
	$Al2p_{3/2}$	74.62	1.5	Al^{3+} (Al_2O_3)	3.85	
	$Al2p_{1/2}$	75.01	1.5	Al^{3+} (Al_2O_3)	3.85	
	O1s	530.95	1.24	Lattice O (Ti–O/Al–O)	39.45	
	O1s-2	532.71	1.73	O-C=O	20.69	
	$Ti2p_{3/2}$-1	459.43	1.11	Ti^{4+}	15.29	
	$Ti2p_{1/2}$-1	465.16	1.87	Ti^{4+}	14.09	
	$Ti2p_{3/2}$-2	472.05	1.12	Ti^{3+}	0.73	
	$Ti2p_{1/2}$-2	458.16	1.88	Ti^{3+}	0.68	
	Ti2p	463.47	2.65	satellite, Ti^{4+}	1.37	
12.5 at% Al_2O_3	C 1s	285.36	1.18	Adventitious C	/	11.6
	$Al2p_{3/2}$	74.46	1.29	Al^{3+} (Al_2O_3)	4.68	
	$Al2p_{1/2}$	74.95	1.29	Al^{3+} (Al_2O_3)	4.68	
	O1s	530.75	1.23	Lattice O (Ti–O/Al–O)	43.06	
	O1s-2	532.52	1.54	O-C=O	11.83	
	$Ti2p_{3/2}$-1	459.24	1.12	Ti^{4+}	17.07	
	$Ti2p_{1/2}$-1	464.95	1.88	Ti^{4+}	15.73	
	$Ti2p_{3/2}$-2	457.96	1.1	Ti^{3+}	0.74	
	$Ti2p_{1/2}$-2	463.07	1.85	Ti^{3+}	0.68	
	Ti2p	471.94	2.72	satellite, Ti^{4+}	1.53	
50 at% Al_2O_3	C 1s	285.36	1.27	Adventitious C	/	40.7
	$Al2p_{3/2}$	74.57	1.27	Al^{3+} (Al_2O_3)	13.72	
	$Al2p_{1/2}$	75.06	1.27	Al^{3+} (Al_2O_3)	13.72	
	O1s	530.99	1.35	Lattice O (Ti–O/Al–O)	32.56	
	O1s-2	532.73	1.75	O-C=O	20.04	
	$Ti2p_{3/2}$-1	459.39	1.2	Ti^{4+}	9.69	
	$Ti2p_{1/2}$-1	465.1	2.01	Ti^{4+}	8.93	
	$Ti2p_{3/2}$-2	457.96	1.05	Ti^{3+}	0.33	
	$Ti2p_{1/2}$-2	463.06	1.76	Ti^{3+}	0.3	
	Ti2p	471.96	2.84	satellite, Ti^{4+}	0.72	

The atomic ratios were calculated from XPS peak areas after calibration using the C 1s peak, with normalization to the Al–O–Ti system. As shown in Table 3, at low doping levels (2.5 and 5 at%), the Al_2O_3/TiO_2 ratio in the film deviates from the target, and the Al content is higher than theoretical. This suggests that Al is prone to surface enrichment during electron beam evaporation at low Al_2O_3 contents, which can be ascribed to the higher Al–O bond energy, different atomic diffusion rates on the substrate, and preferential adsorption of Al species.

At a raw material doping of 12.5 at%, the film exhibits an Al_2O_3/TiO_2 ratio of 11.6 at%, which is close to the nominal composition, indicating stable component transfer under this condition.

At a high doping level of 50 at%, the measured Al_2O_3/TiO_2 ratio decreases to 40.7 at%, lower than the designed value. This is mainly caused by the preferential evaporation of TiO_2 from the mixed source. TiO_2 has higher vapor pressure and lower thermal stability than Al_2O_3, leading to more intense evaporation of Ti-containing species. As a result, the relative deposition amount of Ti is increased, thus reducing the Al_2O_3 fraction in the film and showing typical non-stoichiometric transfer behavior during multi-component oxide evaporation.

3.3. Effect of Al_2O_3 Doping on Optical Properties of TiO_2 Films

3.3.1. Film Transmittance, Refractive Index and Extinction Coefficient

The transmittance curves of TiO_2 films doped with different Al_2O_3 contents in the wavelength range of 300–800 nm (Figure 7) show that all films have high transmittance in the visible region, and the transmittance changes slightly with the increase in Al_2O_3 doping content, indicating that Al_2O_3 doping does not significantly reduce the light transmittance of TiO_2 films, which is beneficial to their application in optical devices.

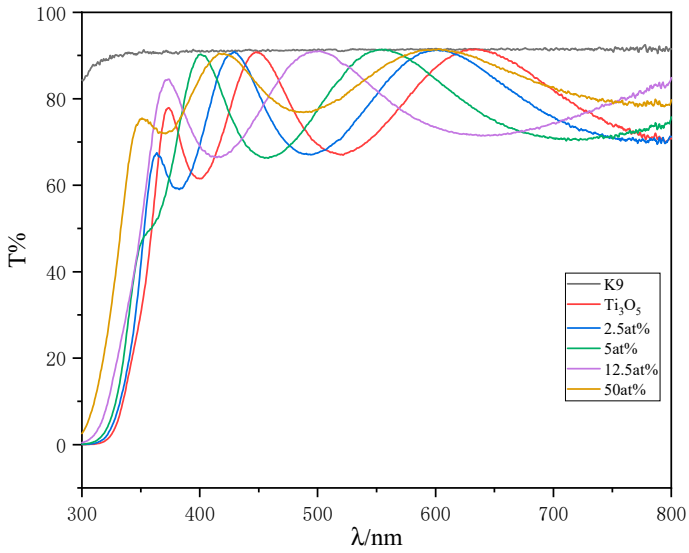


Figure 7. Transmittance curves of Al_2O_3-doped TiO_2 films on K9 glass.

Based on the film transmittance test results, the refractive index (n) and extinction coefficient (k) of the film at 550 nm were fitted and calculated by the Cauchy formula [12] (Formula (2)) and the Exponential model [13] (Formula (3)), and the film thickness was also obtained by fitting. The fitting results are shown in Table 4.

$$n(\lambda) = A_0 + A_1/\lambda^2 + A_2/\lambda^4 \quad (2)$$

$$k(\lambda) = B_1 \exp(B_2\lambda^{-1}) \quad (3)$$

where n(λ) and k(λ) represent the refractive index and extinction coefficient at the corresponding wavelength λ (nm), respectively; A_0, A_1, A_2, B_1 and B_2 are fitting constants.

Table 4. Optical constants of TiO_2 films at 550 nm with different contents of Al_2O_3.

Evaporation Material	*n*	k	Film Thickness/nm	Root Mean Square Error
Ti_3O_5	2.277	7.34×10^{-4}	283	0.161
2.5at% Al_2O_3-doped Ti_3O_5	2.262	8.55×10^{-4}	268	0.150
5at% Al_2O_3-doped Ti_3O_5	2.246	6.89×10^{-4}	247	0.115
12.5at% Al_2O_3-doped Ti_3O_5	2.180	6.06×10^{-4}	225	0.107
50at% Al_2O_3-doped Ti_3O_5	1.963	2.72×10^{-4}	306	0.162

It can be seen from Table 4 that the refractive index of TiO_2 films decreases continuously with the increase in Al_2O_3 doping content, from 2.277 of the undoped sample to 1.963 of the 50 at% doping sample. For the multi-component mixed dielectric film, the refractive index can be calculated by the formula derived from the Lorentz-Lorenz theory [14] (Formula (4)):

$$n^2 = \sum_{i=1}^{m} \left(\frac{a_i c_i n_i^2}{\rho_i} \right) / \sum_{i=1}^{m} \left(\frac{a_i c_i}{\rho_i} \right) \quad (4)$$

where c_i is the volume concentration of the i-th medium molecule; $a_i = 1/(n_i^2 + 2)$; ρ_i is the density of the i-th medium; n_i is the refractive index of the i-th medium. The refractive index of Al_2O_3 is about 1.65, which is much lower than that of TiO_2 film (2.28). Therefore, with the increase in Al_2O_3 content in the film, decreases following the dielectric mixing rule, which is the main reason for the continuous decrease in the refractive index of the doped TiO_2 film.

For the extinction coefficient of the film, it shows a decreasing trend with the increase in Al_2O_3 doping content after a slight increase at low doping content (2.5 at%). Al_2O_3 is a wide bandgap insulator with a bandgap of about 7.5 eV, which almost does not absorb photons in the ultraviolet-visible region. When Al_2O_3 forms a composite film with TiO_2, it "dilutes" the light absorption of TiO_2, leading to the decrease in the extinction coefficient. At the same time, Al_2O_3 can fill the oxygen vacancies in the TiO_2 lattice, passivate the defect states in the film, and reduce the sub-bandgap absorption caused by the defect states, which further reduces the extinction coefficient of the film and improves the optical transmittance.

3.3.2. Film Surface Morphology and Roughness

The surface morphology and surface roughness (Rq) of TiO_2 films with different Al_2O_3 doping contents were characterized by AFM (Figure 8), and the test results are shown in Table 5.

The results show that the surface roughness of all TiO_2 films prepared under this experimental condition is very small (less than 1.1 nm), indicating that the electron beam evaporation method can prepare TiO_2 films with smooth surface. With the increase in Al_2O_3 doping content, the surface roughness of the film gradually increases from 0.608 nm of the undoped sample to 1.01 nm of the 50 at% doping sample. The increase in surface roughness is due to the precipitation of Al_2O_3 second phase at the film surface at high doping content, which causes slight unevenness of the film surface. It is worth noting that the extinction coefficient of the film shows a decreasing trend with the increase in doping content, which is opposite to the change trend of surface roughness, indicating that the decrease in the extinction coefficient is not caused by the change in surface roughness, but mainly by the "dilution effect" of Al_2O_3 and the passivation of oxygen vacancies.

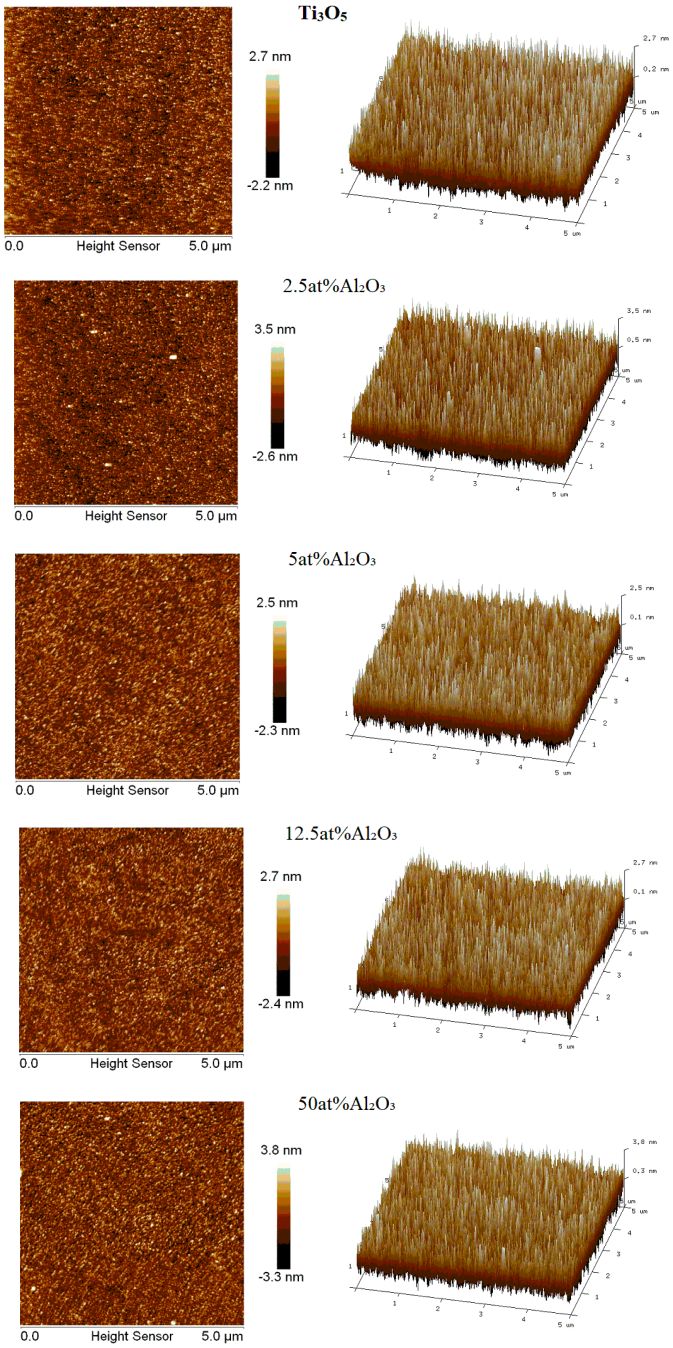


Figure 8. AFM surface morphology images of TiO_2 films with different Al_2O_3 doping contents.

Table 5. Surface Roughness of TiO_2 films with different Al_2O_3 doping contents.

Material	Roughness Rq/nm	Ra/nm	Rmax/nm
Ti_3O_5	0.608	0.480	7.49
2.5at% Al_2O_3-doped Ti_3O_5	0.648	0.496	8.68
5at% Al_2O_3-doped Ti_3O_5	0.695	0.548	8.83
12.5at% Al_2O_3-doped Ti_3O_5	0.709	0.558	8.26
50at% Al_2O_3-doped Ti_3O_5	1.01	0.800	10.4

3.3.3. Film Optical Bandgap

The optical bandgap width of TiO_2 films was calculated based on the ultraviolet-visible transmittance curve. First, the absorption coefficient α of the film at different wavelengths was calculated by Formula (5) [15]:

$$\alpha = \ln(1/T) \times (1/d) \quad (5)$$

where T is the transmittance of the film at the corresponding wavelength; d is the film thickness.

For the semiconductor material with direct optical bandgap, the bandgap width Eg of the material was obtained by extrapolating the linear part of the $(\alpha h\nu)^2$-hν curve to the hν axis (where hν is the photon energy, Figure 9). The calculation results of the optical bandgap width of TiO_2 films with different Al_2O_3 doping contents are shown in Table 6.

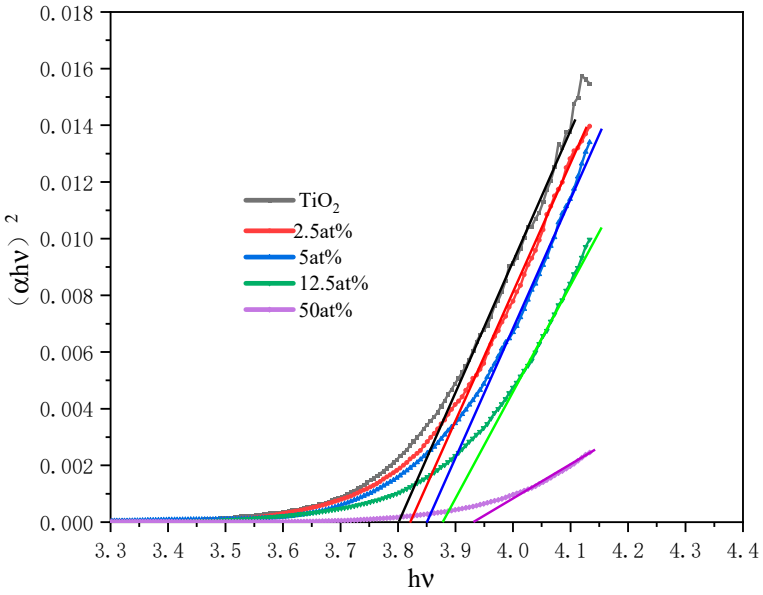


Figure 9. $(\alpha h\nu)^2$ versus hν plots of Al_2O_3-doped TiO_2 films.

Table 6. Optical band gap of TiO_2 thin films with different Al_2O_3 doping contents.

Material	Film Thickness d/nm	Optical Band Gap Eg/eV
Ti_3O_5	283	3.80
2.5 at% Al_2O_3-doped Ti_3O_5	268	3.82
5 at% Al_2O_3-doped Ti_3O_5	247	3.85
12.5 at% Al_2O_3-doped Ti_3O_5	225	3.87
50 at% Al_2O_3-doped Ti_3O_5	306	3.93

It can be seen from Table 5 that the optical bandgap width of TiO_2 films shows an obvious increasing trend with the increase in Al_2O_3 doping content, from 3.80 eV of the undoped sample to 3.93 eV of the 50 at% doping sample, showing a blue shift in the bandgap. The bandgap width of the pure TiO_2 film prepared by electron beam evaporation is 3.80 eV, which is larger than the bulk bandgap width of rutile TiO_2 (3.4 eV), which is mainly due to the quantum size effect of the nanometer-sized TiO_2 film [16]. The quantum size effect of the semiconductor film can be described by Formula (6) [17]:

$$E_g(\mathrm{QD}) = E_g(\mathrm{bulk}) + \left(\frac{h^2}{8R^2}\right)\left(\frac{1}{m_c} + \frac{1}{m_h}\right) - \frac{1.8e^2}{4\pi\varepsilon_0\varepsilon R} \quad (6)$$

where *Eg* (QD) is the bandgap of quantum dots; *Eg*(bulk) is the bandgap of bulk semiconductor; *h* is Planck's constant; *R* is the radius of quantum dots; mc and mh are the effective mass of electrons and holes, respectively; *e* is the elementary charge; ε_0 is the vacuum permittivity; ε is the relative permittivity of the semiconductor material. When the particle size of the semiconductor is small, the quantum confinement effect is dominant, and the positive contribution of the quantum confinement energy term is much greater than the negative contribution of the Coulomb attraction energy term, leading to the increase in the bandgap width of the nanometer-sized film compared with the bulk material.

The further increase in the bandgap width of the TiO_2 film caused by Al_2O_3 doping is mainly due to the lattice compression and strain effect [16]. The ionic radius of Al^{3+} (0.535 Å) is smaller than that of Ti^{4+} (0.605 Å) in the TiO_2 lattice. When Al^{3+} replaces Ti^{4+} in the TiO_2 lattice, it causes the contraction of the TiO_6 octahedral framework and produces compressive strain in the lattice. This compressive strain changes the band structure of TiO_2, usually making the minimum of the conduction band move upward and/or the maximum of the valence band move downward, thus leading to the broadening of the optical bandgap width of the film, which is the main reason for the blue shift in the bandgap of the doped TiO_2 film.

4. Conclusions

Al_2O_3 doping effectively stabilizes λ-Ti_3O_5 at room temperature with complete β→λ phase transition at 5 at%. The composition transfer is most stable at 12.5 at% doping. With increasing Al_2O_3 content, the refractive index and extinction coefficient decrease, while the band gap and surface roughness increase. These changes originate from the low refractive index of Al_2O_3, lattice compressive strain, and oxygen vacancy passivation. This work provides a reliable strategy for preparing stable, high-quality TiO_2 optical thin films.

Author Contributions: Conceptualization, Y.Y.; methodology, C.P. and X.W.; investigation, C.P., X.W. and Z.S.; validation, Z.S. and B.Z.; formal analysis, Y.Y.; visualization, C.P., X.W. and H.D.; writing—original draft preparation, C.P.; writing—review and editing, C.P., X.W., Z.S., H.D. and B.Z.; supervision, Y.Y.; funding acquisition, Y.Y. All authors have read and agreed to the published version of the manuscript.

Funding: This research was funded by the National Key Research and Development Program of China, grant number 2022YFB3504902.

Institutional Review Board Statement: Not applicable.

Informed Consent Statement: Not applicable.

Data Availability Statement: The original contributions presented in this study are included in the article. Further inquiries can be directed to the corresponding authors.

Acknowledgments: The authors thank the National Key Research and Development Program of China for the financial support. The authors also thank the Testing and Analysis Center of GRINM Group Corporation Limited for the characterization of material structure and performance.

Conflicts of Interest: The authors Cheng Peng, Xingqi Wang, Zhixia Shi, Huaying Duan, Bitian Zhang, and Yanxi Yin are employees of GRINM Group Corporation Limited, GRINM Resources and Environment Tech. Co., Ltd. and General Research Institute for Nonferrous Metals. The authors declare that the research was conducted in the absence of any commercial or financial relationships that could be construed as a potential conflict of interest.

Abbreviations

The following abbreviations are used in this manuscript:

XRD	X-ray diffractometer
DSC	Differential Scanning Calorimetry
EDS	Energy Dispersive Spectroscopy
XPS	X-ray Photoelectron Spectroscopy
AFM	Atomic Force Microscopy
UV-Vis	Ultraviolet-visible spectrophotometry

References

1. Duyar, Ö.; Placido, F.; Durusoy, H.Z. Optimization of TiO_2 films prepared by reactive electron beam evaporation of Ti_3O_5. *J. Phys. D Appl. Phys.* **2008**, *41*, 095307. [CrossRef]
2. Nakamura, Y.; Sakai, Y.; Azuma, M.; Ohkoshi, S.I. Long-term heat-storage ceramics absorbing thermal energy from hot water. *Sci. Adv.* **2020**, *6*, eaaz5264. [CrossRef] [PubMed]
3. Shen, Z.; Shi, Q.; Huang, W.; Huang, B.; Wang, M.; Gao, J.; Shi, Y.; Lu, T. Stabilization of microcrystal λ-Ti_3O_5 at room temperature by aluminum-ion doping. *Appl. Phys. Lett.* **2017**, *111*, 191902. [CrossRef]
4. Wang, M.; Huang, W.; Shen, Z.; Gao, J.; Shi, Y.; Lu, T.; Shi, Q. Phase evolution and formation of λ phase in Ti_3O_5 induced by magnesium doping. *J. Alloys Compd.* **2019**, *774*, 1189–1194. [CrossRef]
5. Ahmad, A.A.; Alakhras, L.A.; Al-Bataineh, Q.M.; Telfah, A. Impact of metal doping on the physical characteristics of anatase titanium dioxide (TiO_2) films. *J. Mater. Sci. Mater. Electron.* **2023**, *34*, 15521. [CrossRef]
6. Rehman, I.; Hanif, M.B.; Alghamdi, A.S.; Khaliq, A.; Halim, K.S.A.; Subhani, T.; Motola, M.; Khan, A.F. Intrinsic Properties of Multi-Layer $TiO_2/V_2O_5/TiO_2$ Coatings Prepared via E-Beam Evaporation. *Materials* **2022**, *15*, 3933. [CrossRef] [PubMed]
7. Ogawa, T.; Zhao, Y.; Okumura, H.; Ishihara, K.N. Enhanced Photocatalytic Activity of TiO_2 Thin Film Deposited by Reactive RF Sputtering under Oxygen-Rich Conditions. *Photochemistry* **2022**, *2*, 138–149. [CrossRef]
8. Yang, P.; Xu, Y.; Deng, M.; Li, J.; Chen, Z. Electronic structure, optical properties and elasticity of Ti_3O_5: Insights from first-principles. *Sci. Sin. Phys. Mech. Astron.* **2025**, *55*, 107011. [CrossRef]
9. Okawa, M.; Takegami, D.; Christovam, D.S.; Ferreira-Carvalho, M.; Kuo, C.Y.; Chen, C.T.; Miyoshino, T.; Takasu, K.; Okuda, T.; Chang, C.F.; et al. Linear dichroic x-ray absorption response of Ti-Ti dimers along the c axis in Ti_2O_3 upon Mg substitution. *Phys. Rev. B* **2023**, *108*, 195108. [CrossRef]
10. Greczynski, G.; Hultman, L. Impact of sample storage type on adventitious carbon and native oxide growth: X-ray photoelectron spectroscopy study. *Vacuum* **2022**, *205*, 111463. [CrossRef]
11. Greczynski, G. Binding energy referencing in X-ray photoelectron spectroscopy: Expanded data set confirms that adventitious carbon aligns to the sample vacuum level. *Appl. Surf. Sci.* **2024**, *670*, 160666. [CrossRef]
12. Droulers, G.; Beaumont, A.; Beauvais, J.; Drouin, D. Spectroscopic ellipsometry on thin titanium oxide layers grown on titanium by plasma oxidation. *J. Vac. Sci. Technol. B* **2011**, *29*, 021006. [CrossRef]
13. Shen, W.D.; Liu, X.; Ye, H.; Gu, P.F. A new method for determining thin film thickness and optical constants. *Acta Opt. Sin.* **2004**, *24*, 885–889.
14. Liu, Y. Relationship of refractive index to mass density and self-consistency of mixing rules for multicomponent mixtures like ambient aerosols. *Aerosol Sci. Technol.* **2008**, *39*, 974–986. [CrossRef]
15. Diamantopoulos, N.C.; Barnasas, A.; Garoufalis, C.S.; Anyfantis, D.I.; Bouropoulos, N.; Poulopoulos, P.; Baskoutas, S. Band Gap Measurements of Nanometer Sized Rutile Thin Films. *Nanomaterials* **2020**, *10*, 2379. [CrossRef] [PubMed]
16. Goel, V.; Kumar, Y.; Rawat, G.; Kumar, H. Self-powered photodetectors: A device engineering perspective. *Nanoscale* **2024**, *16*, 9235–9258. [CrossRef]
17. Zhang, X.J.; Zhang, G.F.; Jin, H.X.; Zhu, L.D.; Liu, Q.J. First-principles study of N, Co co-doped anatase TiO_2 photocatalysts. *Acta Phys. Sin.* **2013**, *62*, 013701.

Disclaimer/Publisher's Note: The statements, opinions and data contained in all publications are solely those of the individual author(s) and contributor(s) and not of MDPI and/or the editor(s). MDPI and/or the editor(s) disclaim responsibility for any injury to people or property resulting from any ideas, methods, instructions or products referred to in the content.